Journal of Wind Engineering & Industrial Aerodynamics 230 (2022) 105169

Contents lists available at ScienceDirect

Journal of Wind Engineering & Industrial Aerodynamics

journal homepage: www.elsevier.com/locate/jweia

High-order scale-resolving simulations of extreme wind loads on a model high-rise building

Giorgio Giangaspero [a,*], Luca Amerio [b], Steven Downie [b], Alberto Zasso [c], Peter Vincent [a]

[a] Imperial College London, London, SW7 2AZ, UK
[b] Arup, 8-13 Fitzroy St, London, W1T 4BQ, UK
[c] Politecnico di Milano, Milan, 20133, Italy

ARTICLE INFO

Keywords:
CFD
LES
Extreme wind-loads
High-rise building
High-order

ABSTRACT

Building facade systems can be subject to severe and highly localized wind suction pressures. Such pressures need to be accurately assessed in order to estimate the maximum loads on a typical cladding panel. Wind tunnel experiments studying turbulent flow over a model high-rise building have shown space–time localized peaks of extremely low pressure ($C_p < -8$) on the model building facade. Such low pressure values are unexpected and the potential implications for the cost and carbon intensity of cladding systems are significant. In this work, we use the open-source solver PyFR to carry out high-order Implicit Large Eddy Simulations (ILES) of this test case. The simulations capture, for the first time, the observed space–time localized peaks of extreme low pressure, replicating the experimental findings. The corresponding fluid structures are shown in detail. They are found to be relatively thin and long vortices spinning with an angular velocity approximately normal to the building wall.

1. Introduction

The facade system, inclusive of cladding panels, accounts for approximately 20%–40% of the total construction cost for most high-rise buildings. Part of the cost is driven by the need to withstand space and time dependent wind suction pressures, which must be assessed during the design phase. The wind-induced suction pressures typically exhibit stronger fluctuations near the corners and edges of high-rise buildings' side walls. In these cases, the pressure fluctuations have a strong non-Gaussian behaviour and large negative skewness (Cook, 2016; Peng et al., 2014; Lamberti et al., 2020; Rigo et al., 2020).

For buildings with complex geometries, or where strong interactions with the flow fields around nearby structures and/or terrain are expected, it is common industry practice to carry out wind tunnel testing (European Committee for Standardization, 2005). In relation to cladding design pressures, the objective of wind tunnel testing is to obtain spatially averaged pressures on scales which are relevant to the loading on individual panels. Due to practical limitations, the spatial density of pressure probe locations is not generally sufficient to measure these averaged pressures directly. Filtering is therefore carried out in the time domain and the resulting pressures translated to the spatial domain using an assumed (often linear) relationship (e.g. the TVL equation, which represents standard practice in the UK Lawson, 1976).

Another approach to study wind-induced loads on buildings is to carry out Computational Fluid Dynamics (CFD) simulations, which allow data to be captured at a greater resolution in both space and time with respect to experiments. This allows area-averaged loads, maximum loads and load profiles to be derived directly rather than estimated from pointwise experimental signals. This constitutes the main advantage of CFD over experiments. Furthermore, CFD simulations provide a three-dimensional representation of the flow field surrounding the model building, giving insight on the flow physics causing the pressure fluctuations. Also, CFD simulations can be used earlier in the design phase because geometrical modifications can be more easily taken into account than in the context of an ongoing experimental campaign. However, while experiments are assumed to capture all physics up to the spatial/temporal resolution of the instrumentation, traditional CFD solvers may give inaccurate results due to excessive numerical dissipation and/or turbulence modelling errors. For instance, both Reynolds-Averaged Navier–Stokes (RANS) and unsteady-RANS (URANS) turbulence modelling approaches have been shown to resolve poorly the vortical structures in the wake and in the separation zones around buildings (Thordal et al., 2019; Tominaga et al., 2008; Blocken, 2014). Also (U)RANS may not resolve the smaller spatial scales that are relevant for design. This issue is typically mitigated by adopting higher-fidelity scale-resolving approaches, i.e. by running Large Eddy

* Corresponding author.
E-mail address: g.giangaspero@imperial.ac.uk (G. Giangaspero).

https://doi.org/10.1016/j.jweia.2022.105169
Received 15 December 2021; Received in revised form 19 August 2022; Accepted 7 September 2022
Available online 13 October 2022

(a) Model building in the test section. Reprinted from [14] with permission. Tile A is the one in the top corner.

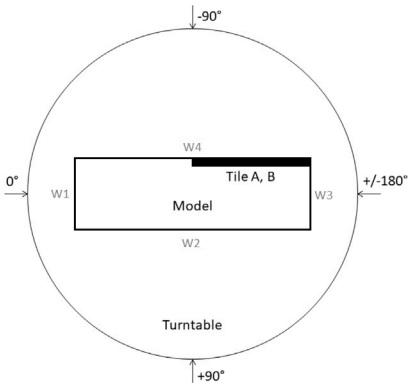

(b) Top view of the turntable, indicating the convention used for the incoming wind direction and for the naming of the building side walls W1 through W4.

Fig. 1. Building model in the Politecnico di Milano wind tunnel.

Simulations (LES), which however increase substantially the computational power/time required. Furthermore, a faithful representation of the incoming turbulence has proven to be of paramount importance for the accuracy of CFD predictions when compared to experiments, see for instance (Aboshosha et al., 2015; Ricci et al., 2018; Thordal et al., 2019; Lamberti and Gorlé, 2020). This requirement limits the use of hybrid RANS/LES approaches, like Detached Eddy Simulations (DES), which have lower computational costs than LES but whose reliability and accuracy for wind engineering applications is still an open question (Thordal et al., 2019). The resulting high computational requirements may force the designer to run CFD simulations for a shorter physical time compared to experiments (Thordal et al., 2019).

Despite the associated technological challenges, CFD simulations have been used successfully in many wind engineering applications. In particular, LES of high-rise buildings have provided predictive values of pressure fluctuations that are comparable to wind tunnel experimental data, see Tamura (2008), Daniels et al. (2013), Thordal et al. (2020a,b) and Lamberti and Gorlé (2020), albeit without extreme negative pressure peaks.

Recent wind tunnel tests (Amerio, 2017; Lamberti et al., 2020) of a model high-rise building have shown local temporally-varying areas of extremely low pressure ($C_p \approx -6 \text{ to } -10$) on the leeward facade of the model building for certain wind directions. To the authors' knowledge, the extreme low-pressure events of the experiments (Amerio, 2017; Lamberti et al., 2020) have not been previously captured by CFD simulations. The phenomenon is unexpected, very localized and time dependent; its flow physics are not fully understood. Designing for pressures in this extreme range has significant implications for the cost and carbon intensity of cladding systems. It is therefore critical to understand the associated spatial characteristics to limit the potential for over-conservative designs. To tackle this problem, here we carry out unsteady high-order Implicit LES (ILES) to study the turbulent flow over the model high-rise building, focusing on the wind direction of 10°. We employ high-order schemes, which are considerably less dissipative than traditional low-order schemes (Vermeire et al., 2017). Furthermore, the ILES approach is taken to reduce the turbulence modelling error typically associated with RANS models. In particular, ILES allow for explicit simulation of vortex structures which govern design pressure loads and are only implicitly represented using RANS methods. We also employ a recent development of the Synthetic Eddy Method (SEM) (Giangaspero et al., 2022) to inject synthetic turbulence and reproduce the incoming turbulent boundary layer that was present in the experiments. In this work, for the first time, we show several extreme low-pressure events and we look at the corresponding turbulent structures in detail.

This paper is organized as follows. The experiments that have shown the presence of very low-pressure peak events are described in Section 2. Section 3 describes the computational method adopted to carry out high-fidelity scale-resolving simulations. Section 4 presents the main results of the numerical simulations. Finally, conclusions are drawn in Section 5 where also the future outlook is presented.

2. Experimental data

2.1. Setup and instrumentation

The experimental studies have been undertaken in the Boundary Layer section of the Politecnico di Milano wind tunnel in collaboration with the Advanced Technology and Research group of Arup UK (Amerio, 2017). The test section has a cross-dimension equal to 14 m x 4 m and a length equal to 35 m (Fig. 1(a)). The model represents a generic high-rise building in scale 1:50, corresponding to a 100 m tall building at full-scale. Its dimensions are $0.3 \times 1 \times 2$ m. The model was tested for several incoming wind directions from −15deg to +30deg and from −135deg to +150deg (Fig. 1(b)). Note that the incoming wind direction corresponds to the angle of attack of the flow relative to the building. This paper focuses on the results obtained with a wind direction equal to +10deg. For this direction strong negative peaks were measured in the leeward top-corner area of the building, i.e. in the area covered by tile A on wall W4 (Fig. 1).

The measurements focused on the regions of the building where the highest peak pressures are expected: two aluminum tiles with 224 pressure taps each were placed in the top corner (tile A) and at the middle of the vertical edge of the model (tile B). The distance between the pressure taps is equal to 3 mm close to the building edges and increases progressively when moving away from the edges (Fig. 2). The model was instrumented with 8 PSI ESP-32 HD high-speed pressure scanners, connected to a data acquisition system with a sampling frequency equal to 500 Hz.

Each wind direction was tested experimentally for 300 s which (assuming a velocity scale equal to ≈ 3) correspond to ≈ 85 min full scale; or $\approx 3100 t_c$, where t_c is the convective time $t_c = L_x/U_\infty$, $L_x = 1$ m is the streamwise length of the model, $U_\infty = 10.3$ m/s is the reference far-field velocity. The Reynolds number was $\text{Re} = \rho_\infty U_\infty L_x/\mu_\infty \approx 6.8 \times 10^5$. The reference velocity is measured by a Pitot tube located

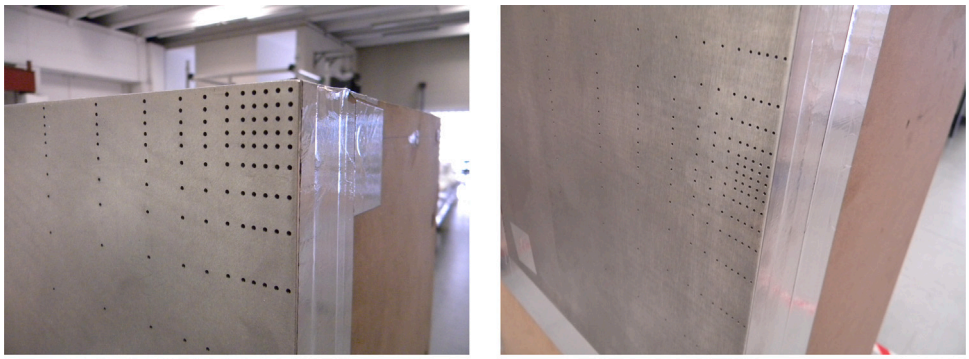

Fig. 2. Detail of the pressure taps close to building's top corner (Tile A) and on building's edge mid-point (Tile B).

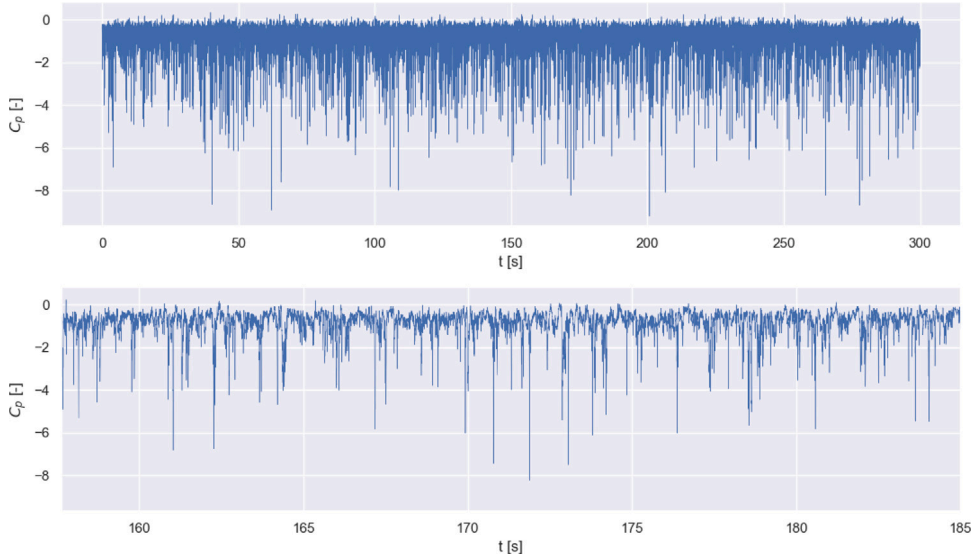

Fig. 3. Experimental pressure time-history recorded for wind direction 10° by a probe of tile A close to the top edge. Top: full time-history. Bottom: detail showing several negative peak events in greater detail.

just upstream to the turntable, 7 m upstream of the model, 1 m above ground. The measured value was then corrected to represent the mean velocity at the centre of the turntable using a previously calculated ratio without the model installed. The reference density ρ_∞ and the reference temperature T_∞ were also measured at the same location. The reference viscosity μ_∞ was determined based on the temperature T_∞.

The same experimental campaign with the same physical model was carried out also in the Wall of Wind wind tunnel of the university of Florida International University, an open-jet wind tunnel with a 4.2 m x 6.1 m wide test-section, and similar results were obtained (Lamberti et al., 2020).

Both experiments recorded severe pressure-peaks events occurring in the leeward top-corner area of the building for a wind direction equal to 10deg, corresponding to the area covered by tile A. For instance, we show the time-history of the pressure signal recorded by a probe close to the top edge, Fig. 3. On a given probe, these events had a relatively low occurring frequency, being recorded on average every 80 to 100 convective times (for $Cp \leq -6$). These phenomena are very localized in space and time dependent.

2.2. Flow conditions

Previous studies (Rocchi et al., 2011; Zasso et al., 2009) have shown that a correct reproduction of the incoming turbulence is essential to correctly simulate the pressure field acting on a structure. The target turbulent boundary layer was chosen to be representative of a typical sub-urban atmospheric boundary layer (ABL) profile. This was achieved using passive turbulence generators at the inlet of the test section (a group of nine 2.5 m tall spires) and roughness elements (bricks) on the wind tunnel floor upstream of the model, see Fig. 1(a).

Prior to the tests, the mean velocity profile, turbulence intensity profile, the characteristic turbulent length scales in the streamwise direction, and the frequency spectrum were measured at 5 different spanwise locations, spaced 0.6 m and symmetrically arranged with respect to the centre of the turntable. 20 s time histories of the three velocity components have been recorded using 3D hot-wires with a sampling frequency of 2000 Hz. The experimental data is reported in Amerio (2017) and Lamberti et al. (2018, 2020) (see also Section 3.2.1). Comparison of the experimental mean velocity profile $U(y)$ to a typical logarithmic mean velocity profile indicates that up to 2.4 m height good agreement is obtained for a roughness length of 1 mm model-scale, corresponding to a z_0/H value of $5 \cdot 10^{-4}$ (see Fig. 5(a)). The integral length scales have been computed using Taylor's hypothesis, taking the product between the mean stream-wise velocity and the streamwise integral time scale of the given velocity component. The streamwise integral time scale is obtained by integrating from 0 to infinity a decaying exponential fitted to the normalized auto-correlation function. The normalized experimental spectrum is in good agreement with the Von Kàrmàn spectrum across the entire range of

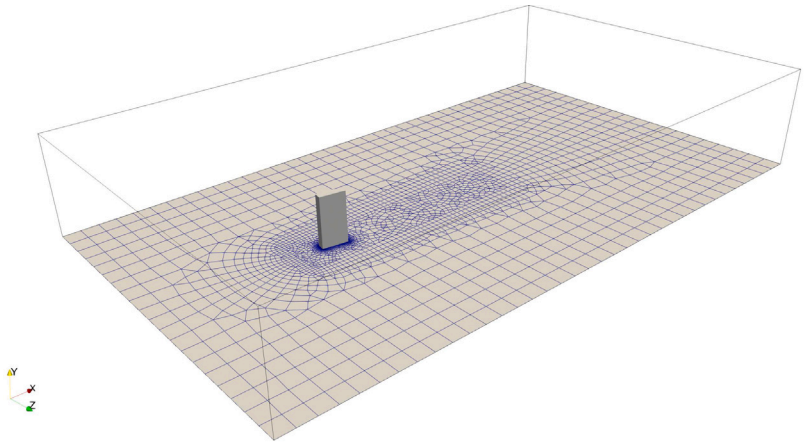

(a) Computational domain and ground mesh

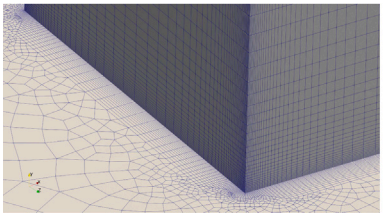

(b) Boundary layer mesh, ground

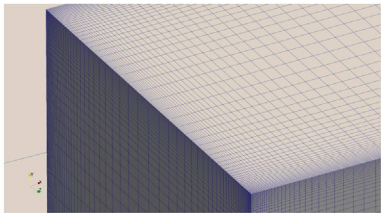

(c) Top of the model building

Fig. 4. Computational domain and mesh.

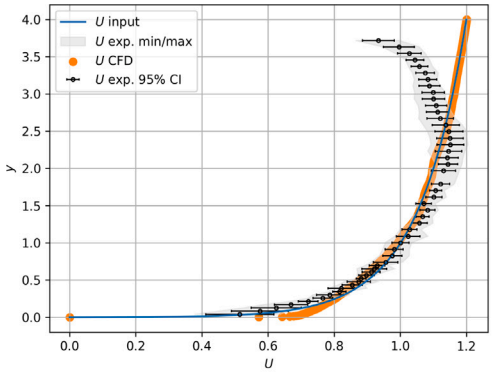

(a) Average velocity profile

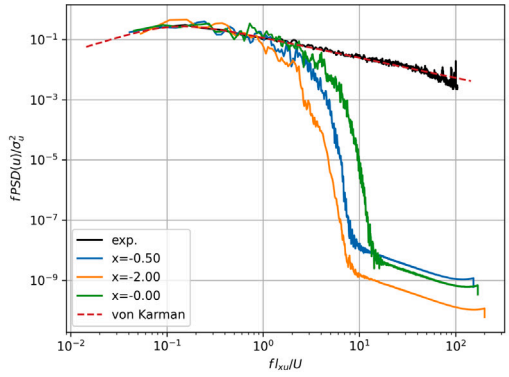

(b) Frequency spectrum at $y = 1$m

Fig. 5. Average profile and frequency spectrum of u at the model location.

frequencies (see Lamberti et al., 2020). The Von Kàrmàn spectrum is given by Lamberti et al. (2020) and Harris (1990):

$$\frac{f\ PSD(u)}{\sigma_u^2} = \frac{4\nu}{\left(1+70.8\nu^2\right)^{5/6}} \tag{1}$$

where

$$\nu = f l_{xu}/U \tag{2}$$

$PSD(u)$ is the power spectrum density of the streamwise instantaneous velocity u, f the dimensional frequency, l_{xu} is the streamwise integral (characteristic) length scale of u, σ_u^2 is the variance of the signal u and U is its mean.

3. Computational method

3.1. PyFR

In this study we utilize the incompressible solver within the open-source Python-based PyFR (www.pyfr.org) (Loppi et al., 2018) framework. The incompressible solver is based on the unsteady artificial compressibility formulation with dual time stepping; convergence is accelerated with a p-multigrid, locally adaptive pseudo-time stepping, and optimal Runge–Kutta schemes. The physical time integration scheme is the standard 2nd-order Backward Differencing Formula (BFD2). The ILES approach has been adopted, thus no explicit sub-grid scale model is used. ILES is based on the hypothesis that the action of the subgrid scales on the resolved scales is equivalent to a strictly dissipative action (Garnier et al., 2009), which is accounted for by the numerical dissipation of the discretization scheme. The solver is high-order accurate in space via the Flux Reconstruction approach (Huynh, 2007) and massively parallel via platform-unified runtime code generation using the MPI + X approach, where X can be OpenMP for conventional CPUs, CUDA for Nvidia GPUs or OpenCL for AMD GPUs.

3.2. Setup

The cross section of the computational domain is the same as the cross section of the wind tunnel (4×14 m) where the experiments were

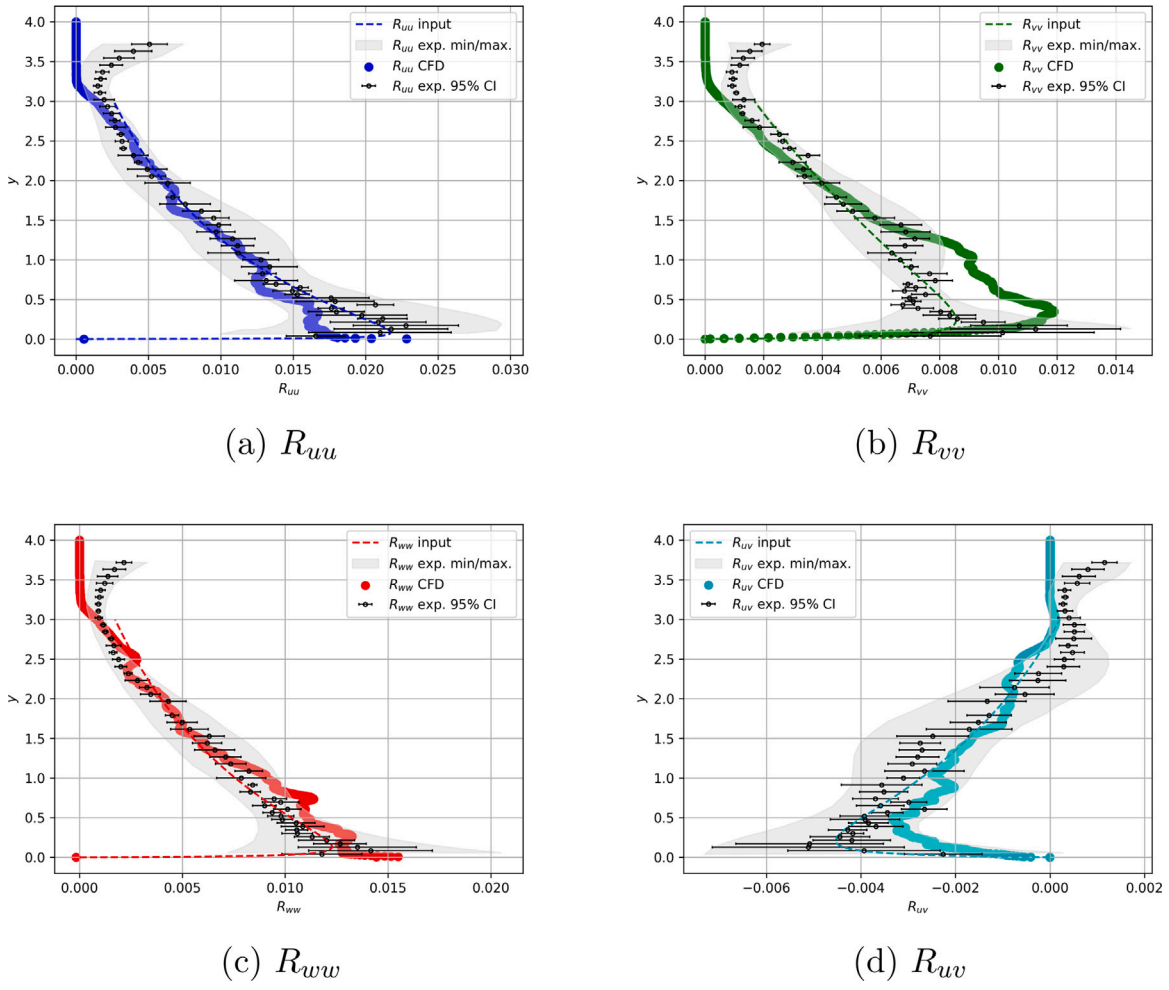

(a) R_{uu} (b) R_{vv}

(c) R_{ww} (d) R_{uv}

Fig. 6. Reynolds stress components.

carried out, see Fig. 4. The origin of the coordinate system is located at the centre of the base of the building, on the ground. The x, y and z directions correspond to the streamwise, vertical, and lateral directions, respectively. The model building dimensions are $1 \times 2 \times 0.3$ m. The inlet and outlet of the domain are located 7 m upstream ($x = -7$) and 17.5 m downstream ($x = 17.5$) of the model building, respectively. The computational mesh consists of 237144 prisms and 1881532 hexahedra for a total of $\approx 2.1 \times 10^6$ elements. The first solution point away from the wall is at $y^+ \approx 1$ (see Fig. 4(b)) for a 4^{th}-order solution polynomial, $p = 4$. Elements are clustered in the vicinity of the model building and in its wake region. Furthermore, the building surface is discretized with a non-uniform structured grid that is refined close to the corners. The same resolution is used for all corners, see Figs. 4(b) and 4(c).

The top wall of the domain is modelled as an inviscid (slip) wall, the building and the ground are modelled as smooth no-slip walls, while all other boundaries are modelled with far-field type boundary conditions. Far-field boundary conditions are Riemann-invariant characteristic boundary conditions which impose weakly the given values of the velocity vector and pressure (Bassi et al., 2006; Loppi, 2019). The Reynolds number is $\text{Re} \approx 6.7 \times 10^5$ (1.5% less than the experimental one). The incoming flow is laminar, the velocity profile is modelled with a logarithmic function that approximates the time-averaged turbulent incoming flow of the experiments (Fig. 5(a)). The same profile is imposed at all other boundaries modelled with far-field type boundary conditions. Synthetic turbulence is generated via a source term (Giangaspero et al., 2022) active 4 m upstream of the model building, see Section 3.2.1, to reproduce the experimental turbulent boundary layer. As in the experimental setup, the mean flow is parallel to the side walls while the model building is rotated with respect to the building's longitudinal axis to obtain the desired relative wind direction. All the results presented here have been obtained with a relative wind direction of 10°.

The simulation was run in three parts. An initial preliminary run was carried out with a piece-wise constant polynomial approximation of the solution ($p = 0$, which corresponds to a first-order accurate spatial discretization scheme) and without any turbulence injection to remove the initial large transients. Then, at nominally $t/t_c = 0$, the simulation was restarted and the flow was developed up to $t/t_c = 20$ using a first-order polynomial approximation of the solution ($p = 1$, second-order accurate) and with turbulence injection enabled. The simulation was then restarted once again with a fourth-order polynomial approximation of the solution ($p = 4$, fifth-order accurate), which corresponds to approximately $250{\times}10^6$ degrees of freedom per equation, and run until $t/t_c = 50$. Time-averaged statistics, probes data and extreme events were collected over the last $20t_c$ ensuring any transients arising from startup or increasing polynomial degree to be damped.

The simulation was advanced in physical time with the BDF2 integration scheme with a time-step of $\Delta t/t_c = 0.001$. Integration in pseudo-time was carried with the optimal embedded pair Runge–Kutta scheme $RK_{10,11,1}$ described in Vermeire et al. (2020). The results shown here have been obtained by running the code on 128 Nvidia P100 GPUs on PizDaint of the Swiss National Supercomputing Centre, and on Wilkes of Cambridge University. With these settings and hardware, the GPU time was $24h/t_c$. Thus the total computation cost for $30t_c$ was $24 \times 128 \times 30 = 92160$ GPU hours. The simulation diverged on two occasions. In those cases, the simulation was restarted from a previous

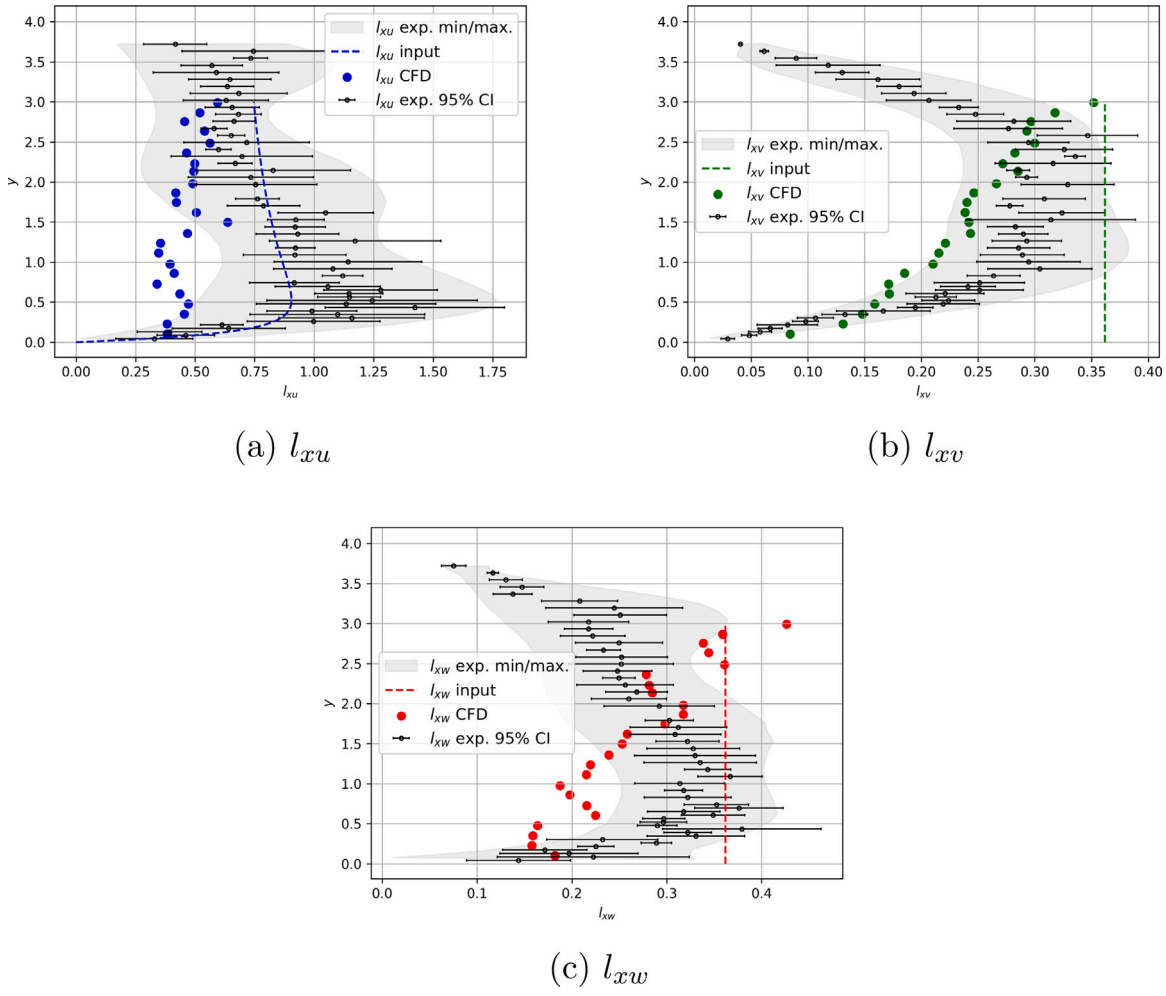

Fig. 7. Stream-wise turbulent (integral) length scales.

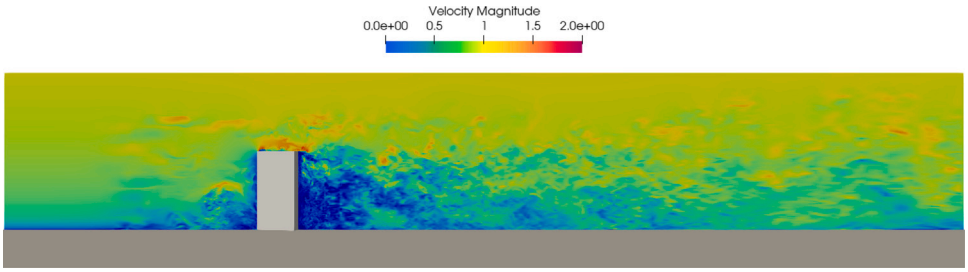

Fig. 8. Velocity magnitude ($|u|/U_\infty$) contours in the plane $z = 0$.

solution and advanced in time with a halved time-step until the time when the simulation previously diverged had been surpassed. Then the simulation was restarted again with the default time-step.

At run time, the pressure at the wall was monitored by $224 \times 4 = 896$ numerical probes which correspond to the pressure probes used in the experiments for tile A for 4 wind directions: $\pm 10°$ and $\pm 170°$. It should be noted that the corresponding experimental data come from four separate, non-simultaneous runs. We also note that the numerical probes record the pressure at a given solution point, thus they are point-wise signals. The experimental probes instead give an area-averaged signal as they measure the pressure over their inlet area, which is finite (Section 2). Each numerical probe recorded a data-point per time-step, which corresponds to a sampling frequency that is 20 times higher than the experimental one. Furthermore, in order to capture the pressure peaks, a conditional writer plugin was developed in PyFR. This plugin wrote the full volumetric solution to file when the local pressure in the area covered by the pressure probes was such that $C_p < -2.8$, with

$$C_p = \frac{p - p_\infty}{\frac{1}{2}\rho_\infty U_\infty^2}, \tag{3}$$

p_∞ being the far-field reference pressure, ρ_∞ the reference density, and U_∞ the reference velocity, i.e. the mean velocity of the undisturbed incoming flow at $y = 1$ m).

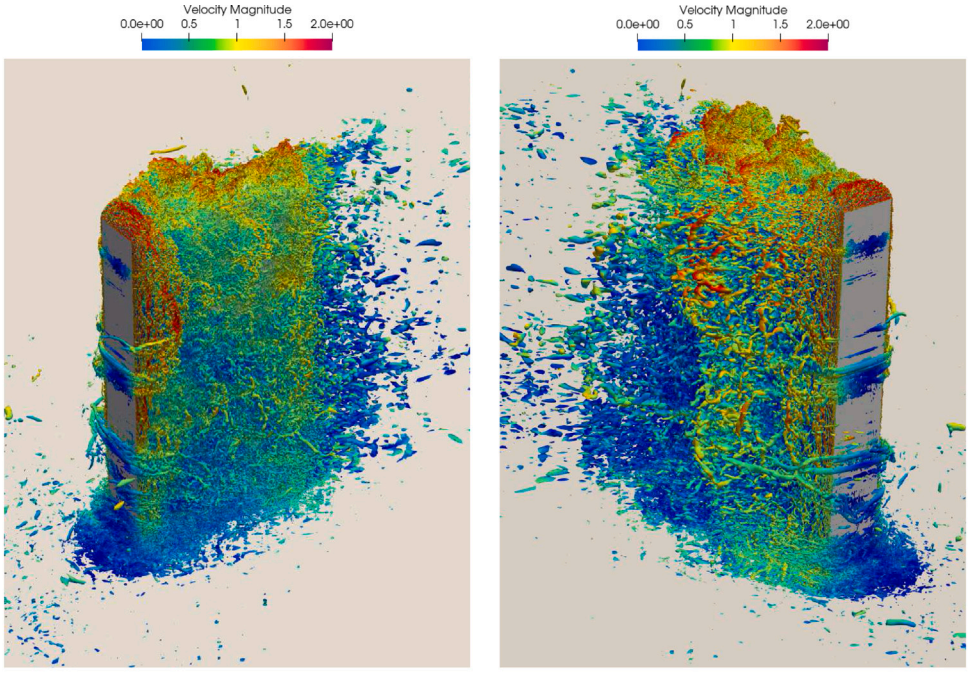

(a) Wall W2 (pressure side, flow is from left to right)

(b) Wall W4 (suction side, flow is from right to left)

Fig. 9. Instantaneous iso-surfaces of the Q-criterion ($Q = 250U_\infty^2/L_x^2$) coloured by the magnitude of velocity ($|u|/U_\infty$). Wind direction of 10°. (For interpretation of the references to colour in this figure legend, the reader is referred to the web version of this article.)

The conditional writer and the synthetic turbulence generation method (see Section 3.2.1) have been implemented in PyFR v1.9.0. A patch that provides the additional functionality used for this work is provided as part of the Supplementary Data. We also provide the mesh and configuration files.

3.2.1. Synthetic turbulence generation

Synthetic turbulence is injected in the computational domain to reproduce the experimental turbulent boundary layer, see Section 2. Synthetic turbulence is generated via a source term following the extended Synthetic Eddy Method (SEM) described in Giangaspero et al. (2022). The source term is added to the right-hand-side of the incompressible Navier–Stokes equations as follows:

$$\frac{\partial u_k}{\partial t} + \nabla \cdot \vec{f}_{u_k} = S_{u_k}, \tag{4}$$

$$S_{u_k} = S_{u_k}(\vec{x}, t) = \begin{cases} \dfrac{u'_k(\vec{x}, t)}{t_k(\vec{x})} \mathcal{F}\left(\vec{x}\right) & \text{if } \vec{x} \in \Omega \\ 0 & \text{if } \vec{x} \notin \Omega, \end{cases} \tag{5}$$

where t_k is characteristic convective turbulent time for velocity component u_k, Ω is the region of space where the turbulence is being generated, $\mathcal{F}$ is a smoothing function, and $u'_k(\vec{x}, t)$ is the fluctuating velocity component, defined according to the classic decomposition:

$$u_k(\vec{x}, t) = U_k(\vec{x}) + u'_k(\vec{x}, t). \tag{6}$$

The signal u'_k is written as a matrix–vector product:

$$u_k(\vec{x}, t) = \sum_j A_{kj}(\vec{x}) \widetilde{u}_j(\vec{x}, t) \tag{7}$$

where A is the Cholesky decomposition of the target Reynolds stress R and $\widetilde{u}_j$ is a signal with zero mean, unit variance and given temporal and spatial correlation. The SEM generates the signal $\widetilde{u}_j$ based on a superimposition of fictitious turbulent eddies with prescribed geometrical shape, random signs and random positions. The eddies are convected with constant velocity across a predetermined region of space, the box of eddies Ω. In this case, the eddies are convected with a velocity equal to U_∞. They influence the flow solution as they travel according to their shape functions and strength, which are designed to obtain the desired Reynolds stress and characteristics turbulent length scales. The field $\widetilde{u}_j(\vec{x})$ is computed as

$$\widetilde{u}_j(\vec{x}) = \sum_{n=1}^{N} \epsilon_{jn} g_j \left(\frac{\vec{x} - \vec{x}_n}{\vec{l}} \right), \tag{8}$$

where ϵ_{jn} is the sign (either $+1$ or -1) of eddy n for component j, and g_j are the shape functions, which is this work are Gaussians. This method ensures that a divergence-free turbulent field is generated. All implementation details can be found in Giangaspero et al. (2022).

The source term formulation allows the box of eddies to be of any size and located anywhere in the domain; it is not constrained to the inlet. In this case, the centre plane of the box of eddies is located 4 m upstream of the model location and covers the area $(0 \le y \le 3) \times (-1.0 \le z \le +1.0)$. A mesh with similar resolution to the one used for the main simulations but without the model building (and its boundary layer) was generated. This coarser mesh consisted of 18400 prisms and 236000 hexes and was used to verify and fine-tune the settings of the synthetic turbulence generator.

We now present a series of figures to show the profile of the mean velocity together with its frequency spectrum (Fig. 5), the profiles of the Reynolds stress components $R_{ij} = \langle u'_i u'_j \rangle$ (Fig. 6), and the profiles of the streamwise characteristic turbulent length scales $l_{xj} = (l_{xu}, l_{xv}, l_{xw})$ (Fig. 7). These results are based on the spanwise- and time-average over $40t_c$ of the flow solution obtained with a third order polynomial approximation of the solution, $p = 3$, on the coarse mesh without the model building. All variables are made non-dimensional appropriately

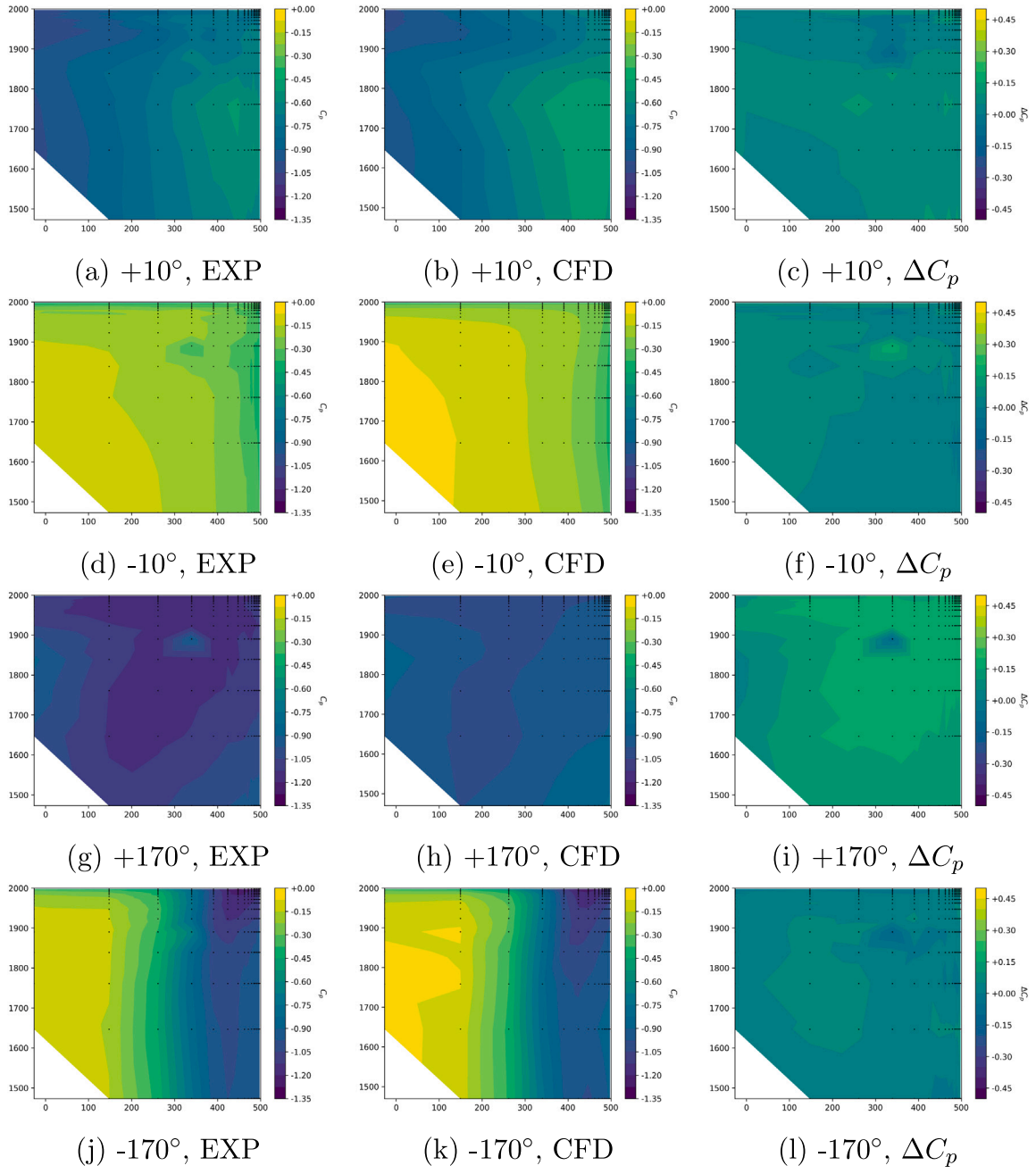

Fig. 10. Mean wind pressure coefficient C_p, comparison between experimental data (EXP) and CFD. $\Delta C_p = C_p^{CFD} - C_p^{EXP}$.

with the reference velocity U_∞. Consistently with experiments, the characteristic integral length scales l_{xj} have been computed by fitting the auto-correlation function of the three velocity components using a decaying exponential and integrating them from 0 to infinity. Where present, the grey area indicates the smoothed spanwise range of the experimental data (minimum/maximum average): it is defined by polynomial fits to the minimum and maximum average values measured across the spanwise locations and thus it is a representation of the spanwise variability. As done in a previous study (Lamberti et al., 2018), the grey area is used as a target region for the numerical results. For completeness, the plots also show the mean experimental values and the corresponding 95% confidence intervals which are defined as $\mu \pm 1.96\sigma/\sqrt{n}$, where μ indicates the mean, σ the standard deviation and $n = 5$ is the number of spanwise locations. The dashed line indicates the input to the turbulence generator. The experimental data relative to the grey area in Figs. 5 to 7 was obtained by digitalizing the corresponding figures in Lamberti et al. (2018).

We focus our attention first on the streamwise velocity u, see Fig. 5. The time-average computational profile of u follows closely the target (input) one, which is an exponential function approximating the experimental profile, see Fig. 5(a). Note that in the CFD the top wall is modelled as a no-slip wall. The frequency spectrum of the velocity signal recorded in the experiments agrees well with the model von-Kármán spectrum of Eq. (1), see Fig. 5(b). The CFD signal at different axial locations is in very good agreement with the experiments in the low and mid frequency range. However, the higher portion of the spectrum is not captured after a cut-off non-dimensional frequency of $\nu = f l_{xu}/U \approx 5$. We note that a similar behaviour was observed also in previous numerical simulations of the same test case with a different synthetic turbulence generation method (the digital filter, Kim et al., 2013; Xie and Castro, 2008), see Lamberti et al. (2018) and Lamberti

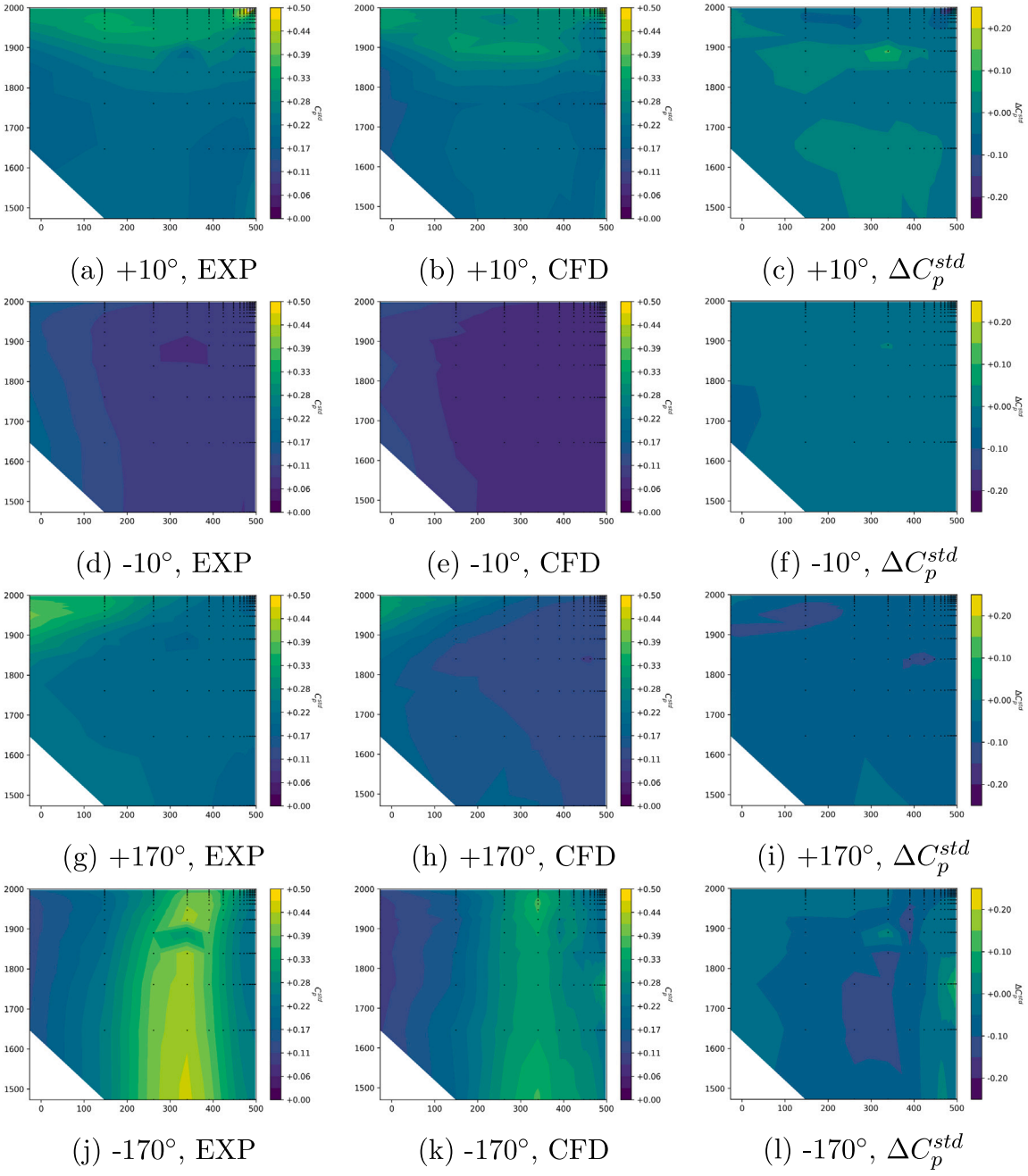

Fig. 11. Standard deviation of wind pressure coefficient, C_p^{std}, comparison between experimental data (EXP) and CFD. $\Delta C_p^{std} = C_p^{std,CFD} - C_p^{std,EXP}$.

and Gorlé (2020). Furthermore, spectra relative to a different test case but with comparable characteristics can be found in Thordal et al. (2019). This lack of resolution in the higher portion of the spectrum can be explained by looking at the mesh resolution. A cut-off non-dimensional frequency of $\nu \approx 5$ indicates that wavelengths smaller than $\lambda_{cut-off} = U/f = l_{xu}/\nu \approx 0.08$ m ($l_{xu} \approx 0.4$ m, see Fig. 7(a)) are not being resolved. The mesh is progressively finer as the location of the model building is approached: the average distance between two solution points in the streamwise direction is 0.05 where turbulence in being injected ($x = -7$) and 0.0125 at the model location ($x = 0$). Thus the minimum wavelength that can be resolved is approximately between $0.0125 \times 2 = 0.025$ and $0.05 \times 2 = 0.1$, i.e. $0.025 < \lambda_{min} < 0.1$. Note that $\lambda_{cut-off}$ falls in this range.

Fig. 6 shows the comparison between the experimental profiles of the non-zero components of the Reynolds Stress R_{ij} and the corresponding profiles measured in the numerical simulations. The turbulence generator covers a height up to $y = 3$ and the top wall is modelled as a slip-wall. Hence the Reynolds stress measured in the CFD solution goes quickly to zero for $y > 3$ while the experimental profiles increase due to the presence of the wind tunnel top wall. Nevertheless, we note that there is a very good agreement between the experimental and numerical results. Similar considerations can be made for the characteristic turbulent (integral) length scales, see Fig. 7, as most of the numerical data points lie within the experimental range. Note that the vertical and spanwise length scales, which have not been measured experimentally, are approximated as follows in the turbulence generator (Amerio, 2017; Lamberti et al., 2018):

$$l_{yu} = 0.2 l_{xu} = l_{yv} = l_{yw}, \tag{9}$$

$$l_{zu} = 0.3 l_{xu} = l_{zv} = l_{zw}. \tag{10}$$

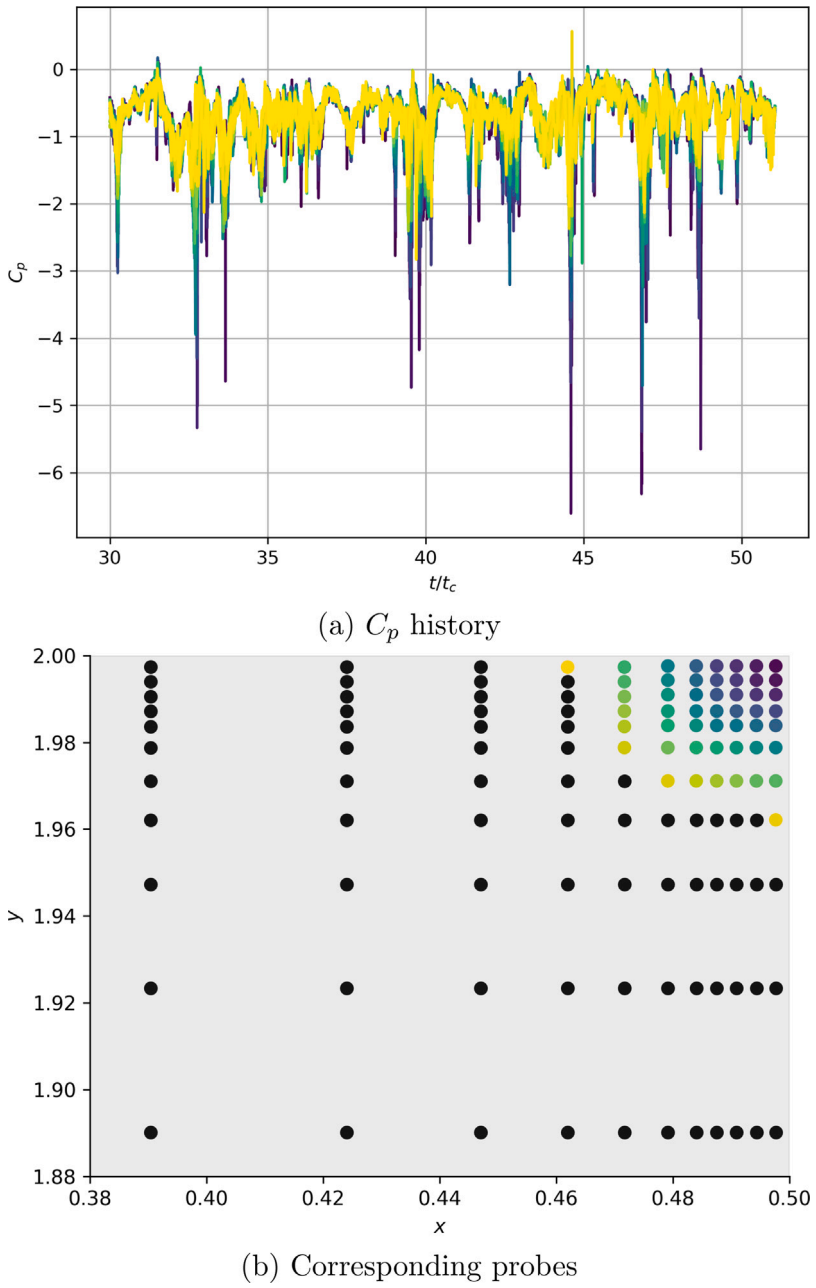

Fig. 12. C_p measured by the 50 numerical probes of tile A closest to the top corner for a wind direction of 10°.

4. Results and discussions

4.1. Flow field

Fig. 8 shows the instantaneous contours of the non-dimensional velocity magnitude $|u|/U_\infty$ in the vertical plane at the centre of the domain. The incoming flow is laminar but turbulence is injected synthetically upstream of the model building as described in Section 3.2.1. The turbulent eddies are convected downstream by the mean flow and later interact with the boundary layer of the model building. As measured in the experiments (Fig. 7(a)), the streamwise extent of the turbulent eddies is similar to that of the model building (1 m). The flow field close to the walls is visualized by means of iso-surfaces of the Q-criterion (Jeong and Hussain, 1995) in Fig. 9. The Q-criterion aims at identifying coherent vortical structures, which are defined as the flow regions where the difference between vorticity magnitude and shear stress magnitude is positive, i.e.:

$$Q = -\frac{1}{2}\sum_{i=1}^{3}\sum_{j=1}^{3}\frac{\partial u_i}{\partial x_j}\frac{\partial u_j}{\partial x_i} > 0, \tag{11}$$

where u_k and x_k ($k = 1, 2, 3$) are the components of the velocity and coordinate vectors, respectively. The model building is characterized by sharp edges which fix the separation point and the transition to turbulence, which is finely resolved, see Fig. 9. On the vertical wall W2 (see Figs. 9(a) and 1(b)), which constitutes the pressure side of the building, the turbulent boundary layer reattaches after a separation region close to the leading edge of the building (i.e. the common edge between walls W1 and W2). The flow on wall W4 (Fig. 9(b)), which is the suction side, is completely separated and thus characterized by a relatively large recirculation region that develops into the wake.

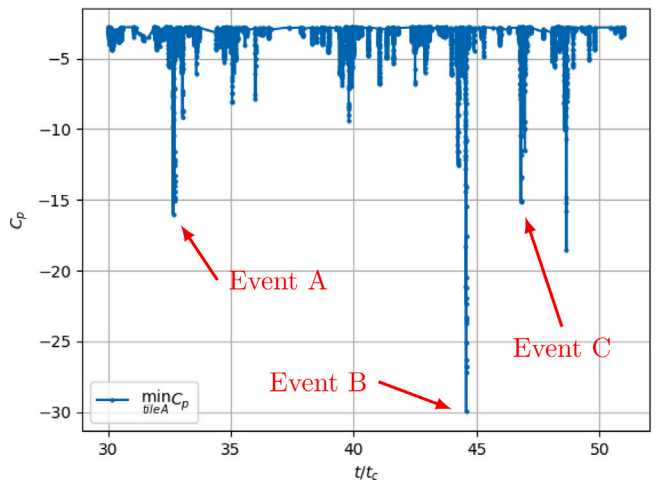

Fig. 13. Minimum C_p measured on the surface area covered by tile A for a wind direction of 10°.

The time-averaged pressure field on tile A can be compared to the one measured by the experiments by looking at the probes data. This is shown in Fig. 10, for 4 wind directions: ±10° and ±170° (see Fig. 1(b) for the definition of the wind direction relative to the building). In this case, the experimental data is taken from the online database (Pomaranzi et al., 2020). The contour levels are obtained by linear interpolation. A very good agreement is found for all wind directions in terms of both trend and absolute values of mean wind pressure coefficient C_p. The local absolute difference between the experimental and numerical data, $|\Delta C_p| = |C_p^{CFD} - C_p^{EXP}|$, is less than 0.45, see the right-most column of Fig. 10. Similarly, the standard deviation of the pressure coefficient, C_p^{std}, is compared in Fig. 11. The trends are well represented by the CFD, but the agreement in terms of absolute values is not as good as for the time-average C_p. The standard deviation of C_p captured by the probes is generally under-predicted by the CFD. This discrepancy can be attributed to the much shorter total sampling time of the CFD compared to the experiments.

Furthermore, we note a consistent disagreement between the CFD results and the experimental ones for the probe located at ($x \approx 350$ mm, $y \approx 1900$ mm), see Figs. 10 and 11. In fact, focusing on the experimental data only, the values of the average C_p and C_p^{std} relative to that probe appear to deviate considerably from the values of the neighbouring probes, which suggests a possible instrumentation issue.

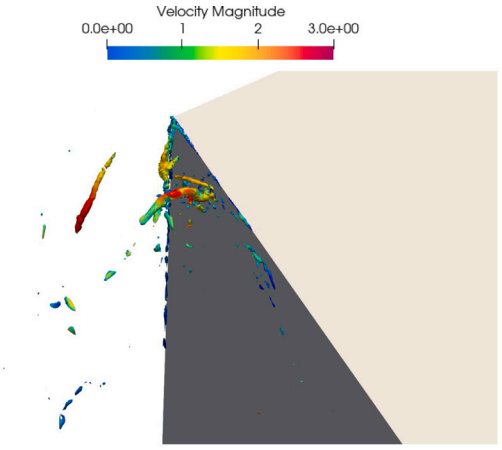

(a) Q, perspective view

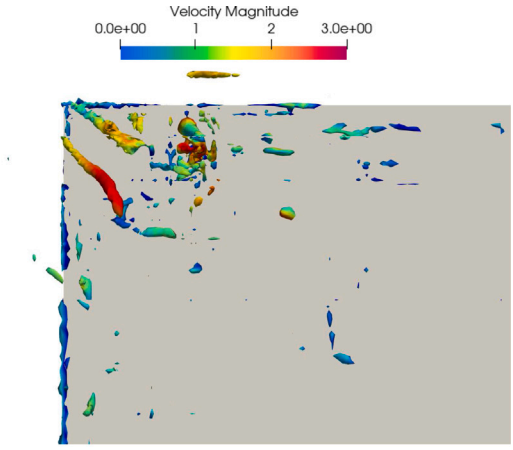

(b) Q, side view

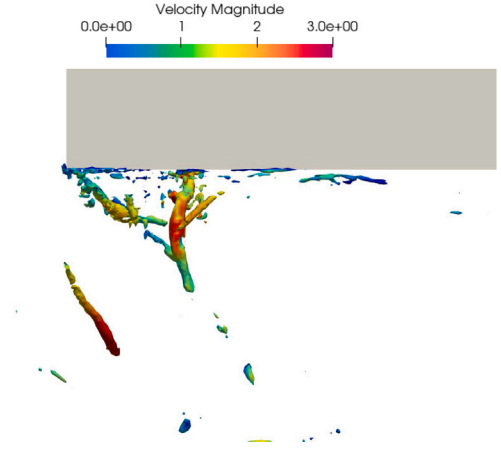

(c) Q, top view

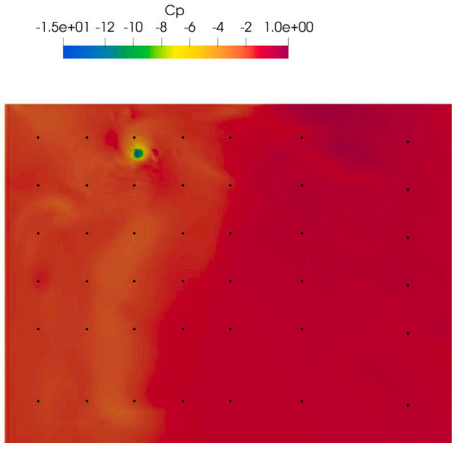

(d) C_p, side view. Black dots indicate the location of the experimental pressure probes

Fig. 14. Event A ($t/t_c \approx 33$, minimum $C_p \approx -16$). Iso-surfaces of the Q-criterion ($Q = 3.25 \times 10^6 U_\infty^2 / L_x^2$) coloured with velocity magnitude (a, b and c) and contours of C_p (d). (For interpretation of the references to colour in this figure legend, the reader is referred to the web version of this article.)

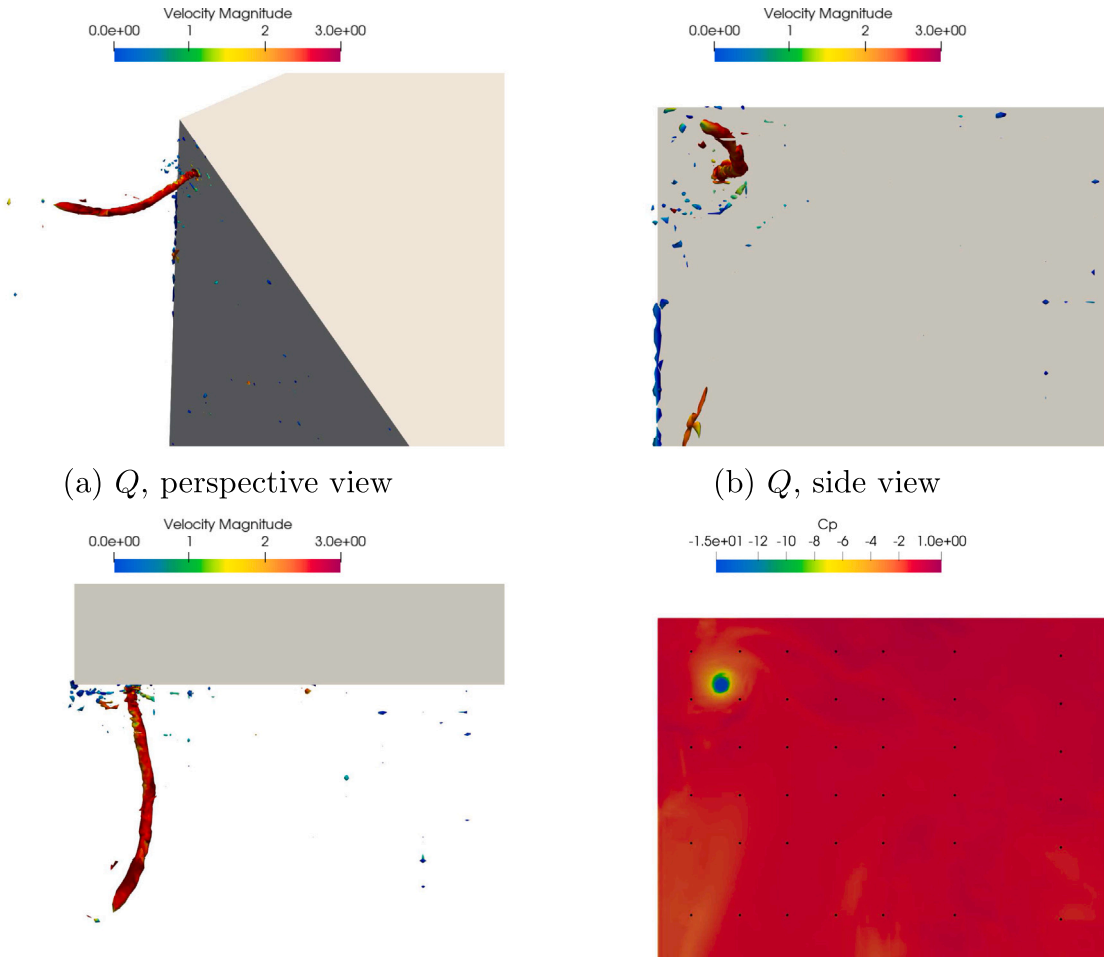

(a) Q, perspective view

(b) Q, side view

(c) Q, top view

(d) C_p, side view. Black dots indicate the location of the experimental pressure probes

Fig. 15. Event B ($t/t_c \approx 45$, minimum $C_p \approx -30$). Iso-surfaces of the Q-criterion ($Q = 7.50 \times 10^6 U_\infty^2 / L_x^2$) coloured with velocity magnitude (a, b and c) and contours of C_p (d). (For interpretation of the references to colour in this figure legend, the reader is referred to the web version of this article.)

4.2. Extreme events

Pressure fluctuations at the wall were monitored at the pressure probes, see Fig. 12, as was the entire surface C_p distribution, the minimum of which is shown in Fig. 13. Both of these time histories were recorded for a wind direction of 10° and were used to identify when extreme events occurred.

The probe data was gathered with the highest possible sampling frequency: a sample point was collected every time step. However, the minimum C_p over the surface area of tile A is a discontinuous signal with non-constant sampling frequency as it was obtained by extracting the solution at the wall from the full volumetric solution written to file by the conditional writer (see Section 3.2). Several severe extreme low-pressure peaks have been observed. The signal recorded by the probes and the minimum C_p have similar behaviour indicating that the physical resolution of the experimental probes is sufficient to detect the occurrence of an extreme event. However, the actual value of C_p recorded with the two approaches is significantly different as the minimum C_p on the surface (Fig. 13) is always considerably lower than the C_p measured by the probes (Fig. 12). For instance, for the first event, occurring at $t/t_c \approx 33$, the probes measured a C_p of ≈ -5 while the minimum C_p on the building surface was ≈ -16. Similarly, for the event at $t/t_c \approx 44.5$, the most extreme one, the C_p measured by the probes was ≈ -6.5 while the minimum C_p on the wall was ≈ -30. This demonstrates how the spatial scale of the minima is smaller than the spacing between the experimental probes.

We now focus our attention on the turbulent structures that generate the extreme fluctuations. In particular, we look at the events A, B and C occurring at $t/tc \approx 33$, $t/tc \approx 45$ and $t/tc \approx 47$, respectively (Fig. 13). The corresponding turbulent structures are shown in Figs. 14 to 16, respectively. Animations of the events are available online as supplemental electronic material.

Each of these three figures contains 4 sub-figures that depict the iso-surfaces of the Q-criterion coloured with velocity magnitude from different point of views (sub-figures a, b and c) and the contours of C_p at the wall (sub-figure d). Note that in Figs. 14 to 16 the flow is from right to left. The vortical structures that generate such pressure peaks are long and thin vortices spinning around an axis almost normal to the leeward building facade. This is especially clear for the most extreme event, Fig. 15. In this case, the value of the Q-criterion (the difference between vorticity magnitude and shear stress magnitude) of the fluid structure was the highest in the domain and thus it was easily isolated. Regarding the other two events, Figs. 14 and 16, the Q-criterion shows the presence of other vortical structures with similar strength (measured in terms of value of the Q-criterion). The bigger one

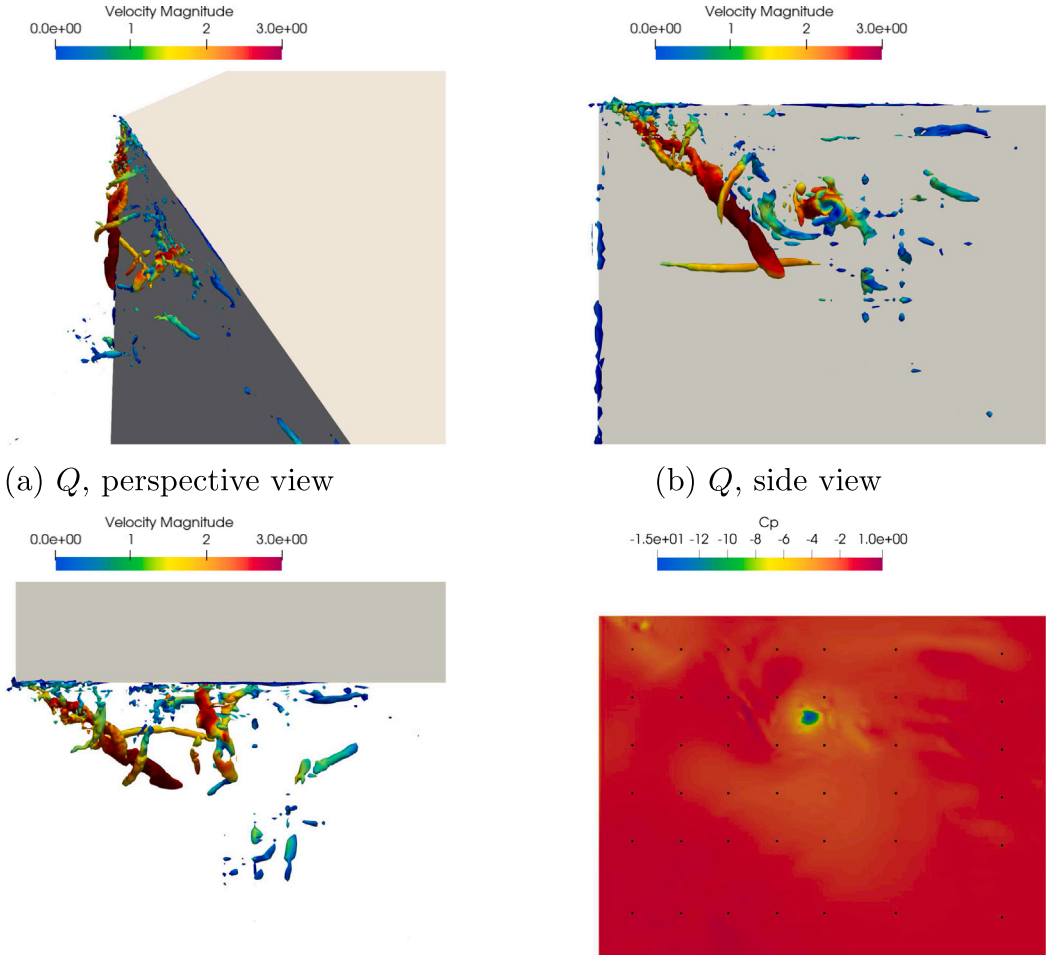

(a) Q, perspective view

(b) Q, side view

(c) Q, top view

(d) C_p, side view. Black dots indicate the location of the experimental pressure probes

Fig. 16. Event C ($t/t_c \approx 47$, minimum $C_p \approx -15$): Iso-surfaces of the Q-criterion ($Q = 3.25 \times 10^6 U_\infty^2 / L_x^2$) coloured with velocity magnitude (a, b and c) and contours of C_p (d). (For interpretation of the references to colour in this figure legend, the reader is referred to the web version of this article.)

is a vortical structure originating from the corner and inclined approximately 45° with respect to the three axis of the wall. Nevertheless, the contours plot of C_p at the wall () show that this type of structure is not responsible for the very low pressure at the wall; instead, that is due to the ones almost normal to the wall. Similar considerations can be made for the other extreme events (not shown here).

5. Conclusions

The turbulent flow over a model high-rise building has been analysed using high-order scale-resolving ILES. Wind tunnel experiments of the same model have shown space–time localized peaks of extremely low pressure ($C_p < -8$) on the building facade for certain wind directions. Such strong fluctuations constitute an unexpected phenomenon that no previous CFD simulations have captured. Yet they are of interest to the wind engineering community for their potential impact on the design of building facades. To replicate the experimental findings, we have carried out CFD simulations of the model high-rise building using the open-source software PyFR, which combines high-order discretization schemes (FR) with the high-fidelity scale-resolving approach of ILES. Synthetic turbulence was injected via a source-term to accurately reproduce the experimental turbulent boundary layer. The wind direction was 10°. Point-wise pressure signals were collected at the same location of the experimental pressure taps. Also, a conditional writer was developed to write the full volumetric solution to disk when a pressure such that $C_p < -2.8$ was detected on the model building surface.

Several extreme low-pressure peak events ($C_p < -10$) have been captured and the corresponding three-dimensional fluid structures have been shown in detail. The most extreme one caused a minimum C_p of ≈ -30. These structures are relatively thin and long vortices spinning with an angular velocity approximately normal to the building wall. The spatial extent of these vortices can be smaller than the spatial resolution of the experimental probes. The location where these structures formed is consistent with the experimental findings, i.e. they appeared close the downstream leeward (suction-side) corner of the building, in particular closer to the top edge rather than to the side one. While the experimental campaigns clearly demonstrated the occurrence of extreme low-pressure events, their spatial extent was unclear due to the limited spatial resolution of the probes. The numerical simulations carried out in this work give important insights into the vortical structures that lead to the low pressure peaks and in particular they allow the designer to estimate more accurately the spatial extent and duration of the low-pressure peaks and thus the expected load on the cladding systems. This in turn limits the potential for over-conservative designs which would have been likely if based only on the experimental results. The

combination of high-order discretization schemes and a high-fidelity scale-resolving approach like ILES has proven successful in resolving this elusive physics.

In future work, extended duration simulations will be undertaken in order to allow quantitative analysis of the frequency at which extreme events are observed. In this context, future work will also investigate whether relatively short-duration simulations, that provide spatially continuous data on the entire building surface, can recover comparable statistics to relatively much longer-duration experiments that only provide data at a finite number of point probe locations. Finally, future work will investigate the genesis of the fluid structures that cause the extreme suction pressures.

CRediT authorship contribution statement

Giorgio Giangaspero: Methodology, Software, Validation, Formal analysis, Investigation, Writing – original draft, Data curation. **Luca Amerio:** Formal analysis, Investigation, Writing – review & editing. **Steven Downie:** Resources, Writing – review & editing. **Alberto Zasso:** Resources, Writing – review & editing. **Peter Vincent:** Conceptualization, Resources, Data curation, Writing – review & editing, Supervision, Project administration, Funding acquisition.

Declaration of competing interest

The authors declare that they have no known competing financial interests or personal relationships that could have appeared to influence the work reported in this paper.

Data availability

Source code and input files provided upon request.

Acknowledgements

The authors would like to thank Freddie Witherden and Niki Loppi for their help with PyFR; Giulia Pomaranzi, Politecnico di Milano, for providing the confidence intervals of the experimental data regarding inlet turbulence; Cambridge University for access to Wilkes and the Swiss National Supercomputing Centre for access to PizDaint. The authors would like to thank the Engineering and Physical Sciences Research Council, UK for their support via an Early Career Fellowship (EP/ K027379/1 and EP/R030340/1).

Appendix A. Supplementary data

Supplementary material related to this article can be found online at https://doi.org/10.1016/j.jweia.2022.105169.

References

Aboshosha, Haitham, Elshaer, Ahmed, Bitsuamlak, Girma T., El Damatty, Ashraf, 2015. Consistent inflow turbulence generator for LES evaluation of wind-induced responses for tall buildings. J. Wind Eng. Ind. Aerodyn. (ISSN: 0167-6105) 142, 198–216. http://dx.doi.org/10.1016/j.jweia.2015.04.004.

Amerio, Luca, 2017. Experimental high resolution analysis of the pressure peaks on a building scale model facades (Ph.D. thesis). Politecnico di Milano, Italy.

Bassi, F., Crivellini, A., Pietro, D.A. Di, Rebay, S., 2006. An artificial compressibility flux for the discontinuous Galerkin solution of the incompressible Navier–Stokes equations. J. Comput. Phys. (ISSN: 0021-9991) 218 (2), 794–815. http://dx.doi.org/10.1016/j.jcp.2006.03.006.

Blocken, Bert, 2014. 50 Years of computational wind engineering: Past, present and future. J. Wind Eng. Ind. Aerodyn. (ISSN: 0167-6105) 129, 69–102. http://dx.doi.org/10.1016/j.jweia.2014.03.008, URL https://www.sciencedirect.com/science/article/pii/S016761051400052X.

Cook, Nicholas J., 2016. Short communication: On the Gaussian-exponential mixture model for pressure coefficients. J. Wind Eng. Ind. Aerodyn. (ISSN: 0167-6105) 153, 71–77. http://dx.doi.org/10.1016/j.jweia.2016.02.009, URL https://www.sciencedirect.com/science/article/pii/S0167610516300010.

Daniels, Steven J., Castro, Ian P., Xie, Zheng-Tong, 2013. Peak loading and surface pressure fluctuations of a tall model building. J. Wind Eng. Ind. Aerodyn. (ISSN: 0167-6105) 120, 19–28. http://dx.doi.org/10.1016/j.jweia.2013.06.014, URL https://eprints.soton.ac.uk/353946/1/JWEAI.pdf.

European Committee for Standardization, 2005. EN 1991-1-4: Eurocode 1: Actions on Structures - Part 1-4: General Actions - Wind Actions. CEN.

Garnier, E., Adams, N., Sagaut, P., 2009. Large Eddy Simulation for Compressible Flows. In: Scientific Computation, Springer Netherlands, ISBN: 9789048128198, URL https://books.google.co.uk/books?id=_7zowRoPSnoC.

Giangaspero, Giorgio, Witherden, Freddie, Vincent, Peter, 2022. Synthetic turbulence generation for high-order scale-resolving simulations on unstructured grids. AIAA J. 60 (2), 1032–1051. http://dx.doi.org/10.2514/1.J061046.

Harris, R.I., 1990. Some further thoughts on the spectrum of gustiness in strong winds. J. Wind Eng. Ind. Aerodyn. (ISSN: 0167-6105) 33 (3), 461–477. http://dx.doi.org/10.1016/0167-6105(90)90001-s.

Huynh, H. T., 2007. A flux reconstruction approach to high-order schemes including discontinuous Galerkin methods. In: 18th AIAA Computational Fluid Dynamics Conference. ISBN: 978-1-62410-129-8, http://dx.doi.org/10.2514/6.2007-4079, URL http://arc.aiaa.org/doi/pdf/10.2514/6.2007-4079.

Jeong, Jinhee, Hussain, Fazle, 1995. On the identification of a vortex. J. Fluid Mech. 285, 69–94. http://dx.doi.org/10.1017/S0022112095000462.

Kim, Yusik, Castro, Ian P., Xie, Zheng-Tong, 2013. Divergence-free turbulence inflow conditions for large-eddy simulations with incompressible flow solvers. Comput. & Fluids (ISSN: 0045-7930) 84, 56–68. http://dx.doi.org/10.1016/j.compfluid.2013.06.001, URL https://eprints.soton.ac.uk/341146/1/cnf2013b.pdf.

Lamberti, Giacomo, Amerio, Luca, Pomaranzi, Giulia, Zasso, Alberto, Gorlé, Catherine, 2020. Comparison of high resolution pressure measurements on a high-rise building in a closed and open-section wind tunnel. J. Wind Eng. Ind. Aerodyn. (ISSN: 0167-6105) 204, 104247. http://dx.doi.org/10.1016/j.jweia.2020.104247.

Lamberti, Giacomo, García-Sánchez, Clara, Sousa, Jorge, Gorlé, Catherine, 2018. Optimizing turbulent inflow conditions for large-eddy simulations of the atmospheric boundary layer. J. Wind Eng. Ind. Aerodyn. (ISSN: 0167-6105) 177, 32–44. http://dx.doi.org/10.1016/j.jweia.2018.04.004.

Lamberti, Giacomo, Gorlé, Catherine, 2020. Sensitivity of LES predictions of wind loading on a high-rise building to the inflow boundary condition. J. Wind Eng. Ind. Aerodyn. (ISSN: 0167-6105) 206, 104370. http://dx.doi.org/10.1016/j.jweia.2020.104370.

Lawson, T.V., 1976. The design of cladding. Build. Environ. 11 (1), 37–38.

Loppi, Niki Andreas, 2019. High-order incompressible computational fluid dynamics on modern hardware architectures (Ph.D. thesis). Imperial College London, UK.

Loppi, N.A., Witherden, F.D., Jameson, A., Vincent, P.E., 2018. A high-order cross-platform incompressible Navier–Stokes solver via artificial compressibility with application to a turbulent jet. Comput. Phys. Comm. (ISSN: 0010-4655) 233, 193–205. http://dx.doi.org/10.1016/j.cpc.2018.06.016, URL http://www.sciencedirect.com/science/article/pii/S0010465518302248.

Peng, Xinlai, Yang, Luping, Gavanski, Eri, Gurley, Kurtis, Prevatt, David, 2014. A comparison of methods to estimate peak wind loads on buildings. J. Wind Eng. Ind. Aerodyn. (ISSN: 0167-6105) 126, 11–23. http://dx.doi.org/10.1016/j.jweia.2013.12.013, URL https://www.sciencedirect.com/science/article/pii/S0167610513002882.

Pomaranzi, Giulia, Amerio, Luca, Zasso, Alberto, 2020. Politecnico di Milano - Wind tunnel test data on high-rise building (1.0) [Dataset]. http://dx.doi.org/10.5281/zenodo.3948348.

Ricci, M., Patruno, L., Kalkman, I., De Miranda, S., Blocken, B., 2018. Towards LES as a design tool: Wind loads assessment on a high-rise building. J. Wind Eng. Ind. Aerodyn. (ISSN: 0167-6105) 180, 1–18. http://dx.doi.org/10.1016/j.jweia.2018.07.009.

Rigo, François, Andrianne, Thomas, Denoël, Vincent, 2020. A de-mixing approach for the management of large negative peaks in wind tunnel data. J. Wind Eng. Ind. Aerodyn. (ISSN: 0167-6105) 206, 104279. http://dx.doi.org/10.1016/j.jweia.2020.104279, URL https://www.sciencedirect.com/science/article/pii/S0167610520301896.

Rocchi, Daniele, Schito, Paolo, Zasso, Alberto, 2011. Investigation on the relation between incoming wind characteristics and surface pressure loads. In: Proceedings of the 13th International Conference on Wind Engineering (ICWE13), July 10-15, 2011, Amsterdam.

Tamura, Tetsuro, 2008. Towards practical use of LES in wind engineering. J. Wind Eng. Ind. Aerodyn. (ISSN: 0167-6105) 96 (10–11), 1451–1471. http://dx.doi.org/10.1016/j.jweia.2008.02.034.

Thordal, Marie Skytte, Bennetsen, Jens Chr, Capra, Stefano, Koss, H. Holger H., 2020a. Towards a standard CFD setup for wind load assessment of high-rise buildings: Part 1 – Benchmark of the CAARC building. J. Wind Eng. Ind. Aerodyn. (ISSN: 0167-6105) 205, 104283. http://dx.doi.org/10.1016/j.jweia.2020.104283.

Thordal, Marie Skytte, Bennetsen, Jens Chr, Capra, Stefano, Kragh, Andreas K., Koss, H. Holger H., 2020b. Towards a standard CFD setup for wind load assessment of high-rise buildings: Part 2 – Blind test of chamfered and rounded corner high-rise buildings. J. Wind Eng. Ind. Aerodyn. (ISSN: 0167-6105) 205, 104282. http://dx.doi.org/10.1016/j.jweia.2020.104282.

Thordal, Marie Skytte, Bennetsen, Jens Chr., Koss, H. Holger H., 2019. Review for practical application of CFD for the determination of wind load on high-rise buildings. J. Wind Eng. Ind. Aerodyn. (ISSN: 0167-6105) 186, 155–168. http://dx.doi.org/10.1016/j.jweia.2018.12.019.

Tominaga, Yoshihide, Mochida, Akashi, Murakami, Shuzo, Sawaki, Satoshi, 2008. Comparison of various revised $k - -\epsilon$ models and LES applied to flow around a high-rise building model with 1:1:2 shape placed within the surface boundary layer. J. Wind Eng. Ind. Aerodyn. (ISSN: 0167-6105) 96 (4), 389–411. http://dx.doi.org/10.1016/j.jweia.2008.01.004, URL https://www.sciencedirect.com/science/article/pii/S0167610508000020.

Vermeire, Brian C., Loppi, Niki A., Vincent, Peter E., 2020. Optimal embedded pair Runge-Kutta schemes for pseudo-time stepping. J. Comput. Phys. (ISSN: 0021-9991) 415, 109499. http://dx.doi.org/10.1016/j.jcp.2020.109499.

Vermeire, B.C., Witherden, F.D., Vincent, P.E., 2017. On the utility of GPU accelerated high-order methods for unsteady flow simulations: A comparison with industry-standard tools. J. Comput. Phys. (ISSN: 0021-9991) 334, 497–521. http://dx.doi.org/10.1016/j.jcp.2016.12.049, URL http://spiral.imperial.ac.uk/bitstream/10044/1/43590/11/1-s2.0-S0021999116307136-main.pdf.

Xie, Zheng-Tong, Castro, Ian P., 2008. Efficient generation of inflow conditions for Large Eddy simulation of street-scale flows. Flow Turbul. Combust. (ISSN: 1386-6184) 81 (3), 449–470. http://dx.doi.org/10.1007/s10494-008-9151-5, URL https://eprints.soton.ac.uk/52402/1/efficient_generation_of_inflow_conditiosn_for_large_eddy_simulation_of_street-scale_flows_ztx_and_ipc.pdf.

Zasso, Alberto, Rocchi, Daniele, Schito, Paolo, 2009. Experimental and numerical study of the flow around a low rise building. In: 5th European & African Conference on Wind Engineering (EACWE5). pp. 1–9.